

Supporting Information

Hollow CoP spheres assembled by porous nanosheets as high-rate and ultra-stable electrode for advanced supercapacitors

Li Sun,^{a,b,c} Zhenbin Xie,^c Aiping Wu,^b Chungui Tian,^{b*} Dongxu Wang,^b Ying Gu,^b
Yachen Gao,^{a*} and Honggang Fu^{b*}

^aKey Laboratory of Electronics Engineering, College of Heilongjiang Province, Heilongjiang University, Harbin 150080, Cina.

^bKey Laboratory of Functional Inorganic Material Chemistry, Ministry of Education of the People's Republic of China, Heilongjiang University, Harbin 150080, P. R. China.

^cChemistry and Chemical Engineering Institute, Qiqihar University, Qiqihar 161006, China

Email: gaoyachen@hlju.edu.cn, chunguitianhq@163.com, fuhg@vip.sina.com

The content of ESI

1. Experimental section.

2. **Figure S1.** SEM images of Co-EG-10 precursor after sonication for 3h at high power of 120 W.
3. **Figure S2.** XRD pattern of the Co-EG-10 precursor.
4. **Figure S3.** SEM images of (a, b) HCPS-10-300 and (c, d) HCPS-10-400.
5. **Figure S4.** XRD pattern of HCPS-10-300, HCPS-10-350 and HCPS-10-400.
6. **Figure S5.** N₂ adsorption/desorption isotherms and pore size distribution (inset) of (a) HCPS-10-300 and (b) HCPS-10-400.
7. **Figure S6.** SEM images of (a) Co-EG-4, (b) Co-EG-6, (c) Co-EG-8 and (d) Co-EG-12.
8. **Figure S7.** (a, b) SEM images; (c) XRD pattern and (d) N₂ adsorption/desorption isotherm and pore size distribution (inset) of the Co₃O₄.
9. **Figure S8.** Electrochemical performance of the Co₃O₄ using a three-electrode system in 2 M KOH electrolyte: (a) CV curves of Co₃O₄ electrode at various scan rate from 10 mV s⁻¹ to 100 mV s⁻¹; (b) The plot of log *i* vs log *v* of Co₃O₄ electrode at different redox states; (c) Capacitive and diffusion-controlled charge storage contribution of Co₃O₄ electrode at 20 mV s⁻¹; (d) Charge storage contribution ratio of at different scan rates for Co₃O₄ electrode.
10. **Figure S9.** (a) CV curves of HCPS-4, HCPS-6, HCPS-8 and HCPS-12 at 20 mV s⁻¹ in the voltage range of -0.2~0.5 V; (b) GCD curves of HCPS-4, HCPS-6, HCPS-8 and HCPS-12 at 1 A g⁻¹ in the voltage range of -0.2~0.5 V.
11. **Figure S10.** (a) Specific capacitance of the HCPS-10-350 coated Ni foam electrodes as a function of the mass loading of HCPS-10-350 sample; (b) Specific capacitance as a function of current density ranging from 1 to 30 A g⁻¹.
12. **Figure S11.** XRD patterns of the HCPS-10-350 coated on Ni foam before and after 50,000 GCD cycles.
13. **Figure S12.** (a) Survey XPS spectra of the HCPS-10-350 coated on Ni foam before and after 50,000 GCD cycles, the high-resolution XPS spectra of (d) Co 2p, (e) P 2p and (f) O 1s of the HCPS-10-350 coated on Ni foam before and after cycling.

14. **Figure S13.** The cycle stability of the HCPS-4, HCPS-6, HCPS-8 and HCPS-12 electrode measured at a current density of 10 A g^{-1} for 50000 cycles.

15. **Figure S14.** The structural and capacitive analyses for BNGC electrode material: (a) TEM image of BNGC; (b,c) HRTEM images of selected areas of (a); (d) XRD patterns of BNGC; (e) N_2 adsorption/desorption isotherm and pore size distribution (inset) of BNGC; (f) Survey XPS spectrum of BNGC; (g) CV curves of BNGC at various scan rate from 10 mV s^{-1} to 500 mV s^{-1} ; (h) GCD curves of BNGC at different current densities from 1 A g^{-1} to 20 A g^{-1} ; (i) Cycle stability and Coulombic efficiency of the CoP-10-350 electrode for 5000 cycles measured at 10 A g^{-1} .

16. **Figure S15.** (a) CV curves of Co_3O_4 //BNGC ASC device at different scan rate from 10 mV s^{-1} to 100 mV s^{-1} ; (b) GCD curves of Co_3O_4 //BNGC ASC device at different current densities from 1 A g^{-1} to 10 A g^{-1} .

17. **Figure S16.** Coulombic efficiency of of the HCPS-10-350 and Co_3O_4 electrode measured at a current density of 10 A g^{-1} for 50000 and 5000 cycles, respectively.

18. **Table S1.** The as-prepared samples and their corresponding synthesis parameters.

19. **Table S2.** Textual parameters of the as-fabricated Co-based samples.

20. **Table S3.** Specific capacitance of the studied samples calculated from discharge curves measured at different current densities.

21. **Table S4.** Comparison of supercapacitive performance of HCPS-10-350 with other previously reported CoP-based electrodes using a three-electrode system.

22. **Table S5.** Comparison of vital capacitive parameters indexes of HCPS-10-350//BNGC ACS device with other previously reported Co-based ACS device.

Experimental section

Preparation of hollow CoP sphere assembled by porous nanosheets (HCPS)

In a typical procedure, 2 mmol $\text{Co}(\text{CH}_3\text{OO})_2$ was dissolved into a mixed solution of ethanol (15 mL) and ethylene glycol (15 mL) in a glass beaker upon stirring. then, the homogeneous solution was transferred and sealed into a 50 mL Teflon-lined stainless-steel autoclave, followed by heating at 180 °C for 10 h. Naturally cooling down to room temperature, the as-prepared products (labeled as Co-EG-10 precursor) was centrifuged and washed with ethanol several times, and then dried at 60 °C for 10 h. To get the CoP hollow sphere assembled with 2D porous nanosheets, the Co-EG-10 precursor (100 mg) and NaH_2PO_2 (500 g) were placed at two separate positions in a porcelain boat with NaH_2PO_2 at the upstream side of the tube furnace. Thereafter, the porcelain boat heated at 350 °C with a ramp rate of 3 °C min^{-1} and maintained at 350 °C for 2 h in an N_2 atmosphere. After natural cooling, the resultant sample was denoted as HCPS-10-350. For comparison, Co_3O_4 was obtained by heating Co-EG-10 precursor at 350 °C for 2 h in air atmosphere. In order to investigate the relationship between structure and supercapacitive performance, a series of control experiments were performed, including changing solvothermal times (4, 6, 8, 10 and 12h) and phosphating temperature (300, 350 and 400°C). The as-prepared sample and corresponding synthetic parameters are listed in Table S1.

Synthesis of B, N-doped graphitic carbon (BNGC)

The B, N-doped graphitic carbon (BNGC) is synthesized based on our previous report. Firstly, 1.0 g of chitosan was dissolved in aqueous FeCl_3 (1M, 30 mL) solution under stirring for 3 h at 50 °C. Then, 2.0 g of boric acid was added to the above solution. After vigorous stirring, the homogeneous mixture was transferred into a Teflon-lined stainless-steel autoclave followed by heating at 180 °C for 12 h. the obtained precipitate was collected and mixed with ZnCl_2 at a mass ratio of 1:4. Subsequently, the as-prepared precursor were treated with controlled pyrolysis at 900 °C for 2h with a heating rate of 5 °C min^{-1} in N_2 atmosphere, followed by naturally cooling to room temperature. the sample was treated with hydrochloric acid (1M, 100 mL) for 6 h. Finally, the sample was washed with hot water several times to remove

excess boric oxide and then dried at 80°C overnight. The BNGC was obtained.

Structural characterization

The scanning electron microscopy (SEM) test and energy dispersive X-ray spectroscopy (EDX) elemental mapping characterization were conducted on a Hitachi S-4800 instrument at an accelerating voltage at 5KV. Transmission electron microscopy (TEM) was carried out on a JEM-2100 at an accelerating voltage of 200 kV. Powder X-ray diffraction measurement was recorded radiation on a Bruker D8 diffractometer using Cu K α ($\lambda=1.5406 \text{ \AA}$) with an acceleration voltage of 40 kV. The N₂ adsorption/desorption isotherms were obtained using a Micromeritics Tristar II. The samples were outgassed for 10 h at 150 °C under vacuum before the measurements. To determine the compositions and chemical valences of the samples, X-ray photoelectron spectroscopy (XPS) was performed on a VG ESCALAB MKII with Mg K α (1253.6 eV) achromatic X-ray radiation.

Electrochemical measurements

The electrochemical measurements were carried out on a CHI 660E electrochemical workstation using a conventional three-electrode system in 2 M KOH electrolyte. A saturated calomel electrode (SCE) electrode and platinum electrode were used as the reference electrode and counter electrode, respectively. The working electrode was prepared by pasting a slurry including the active materials (95 wt%) and polytetrafluoroethylene (PTFE, 5 wt%) on nickel foam (1 cm \times 1 cm) and dried in a vacuum oven. Afterwards, the electrode was pressured under 10 MPa for electrochemical measurement. The mass loading of active materials on every working electrode is about 6 mg cm⁻². Additionally, the HCPS-10-350 electrodes with different loading amount from 2 mg cm⁻² to 12 mg cm⁻² were also prepared to study relationship between mass loading and rate behaviors. In detail, the supercapacitive properties of the prepared materials were studied by using cyclic voltammetry (CV), galvanostatic charge-discharge (GCD) and electrochemical impedance spectroscopy (EIS) techniques. CV curves were tested at -0.2~0.5 V with different scan rate, GCD curves were performed in the potential of -0.2~0.5 V at different current density. The EIS was carried out at the frequency ranging from 0.01 Hz to 100 kHz under open

circuit potential with 5 mV amplitude. The specific capacitance (C_m) of the electrode was calculated from the discharge curve in the three-electrode system according to the following formula (1)

$$C_m = I\Delta t / (m\Delta V) \quad (1)$$

Where C_m , I , Δt , m and ΔV represent specific capacitance ($F g^{-1}$), the applied current (A), discharge time (s), mass of the active material (g) and operating voltage window (V), respectively.

The Coulombic efficiency (η) can be based according to the formula (2)

$$\eta = t_d / t_c \quad (2)$$

Where t_c and t_d represent the time of charge and discharge, respectively.

Fabrication of asymmetric supercapacitor device

The asymmetric supercapacitor (ASC) device (2032-type coin cell) was assembled by employing as-fabricated Co-based sample and BNGC as the positive and negative electrode materials, respectively, and 2.0 M KOH as the electrolyte. The active material mass of positive and negative electrode was determined based on the principle of charge balance according to the calculation formula (3)

$$m^+ / m^- = (C^- \times \Delta V^-) / (C^+ \times \Delta V^+) \quad (3)$$

Where C ($F g^{-1}$), ΔV (V) and m (g) represent the specific capacitance, the potential window and the mass of electrode material, respectively. + represent positive material, while - represent negative material. The optimized mass ratio between HCPS-10-350 and BNGC can be determined to be approximately 1:1.62 based on the above equation. In HCPS-10-350//BNGC ASC device (2032-type coin cell), the mass loading of HCPS-10-350 and BNGC are 18 mg and 29 mg, respectively.

For ACS device, the specific capacitance, power and energy densities were calculated based on the total mass of positive and negative electrode. The specific capacitance of ASC device was calculated using formula (4)

$$C_{cell} = I\Delta t / (m\Delta V) \quad (4)$$

The energy density (E) and power density (P) was calculated according to the following formulas :

$$E = 1/2 C_{cell} V^2 \quad (5)$$

$$P = E/\Delta t \quad (6)$$

Where C_{cell} is the total cell specific capacitance (F g^{-1}), I is the discharge current (A), V is the cell-operation potential (V) and Δt is the discharge time (s).

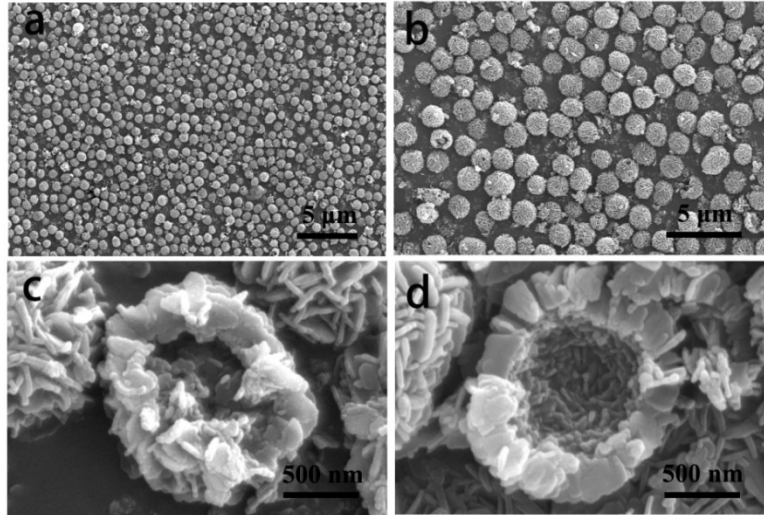


Figure S1. SEM images of Co-EG-10 precursor after sonication for 3h at high power of 120 W.

By the sonication for 3h at high power of 120 W, the SEM images (Figure S1) clearly exhibits the interior structure of the Co-EG-10 precursor. We can see that broken spheres display the hollow interior. Moreover, the hollow spheres are made up of many nano-sheet units with a thickness about several ten nanometers.

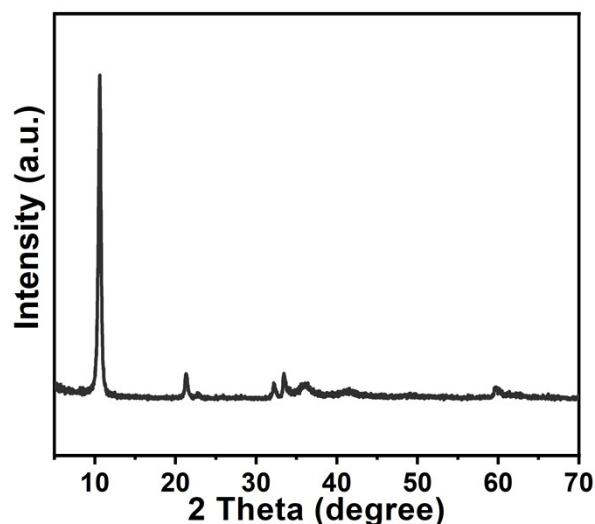


Figure S2. XRD pattern of the Co-EG-10 precursor.

Figure S2 shows the XRD pattern of the Co-EG-10 precursor. The distinct diffraction peak located at around 11° is characteristic of crystalline Co-glycolate complex.

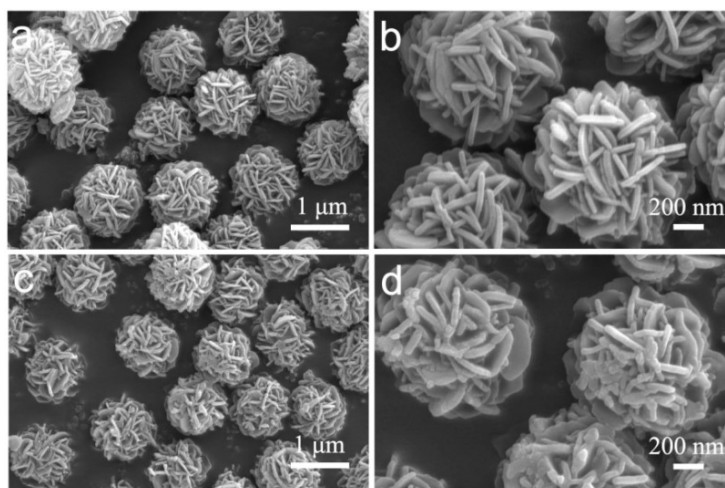


Figure S3. SEM images of (a, b) HCPS-10-300 and (c, d) HCPS-10-400.

The micro-structure of as-prepared materials can be tuned by changing phosphorization temperature. Figure S3a and S3b depict the SEM images of HCPS-10-300 obtained by treating Co-EG-10 at 300°C . The morphology of HCPS-10-300 doesn't change in comparison with that of Co-EG-10. With the temperature elevated to 400°C , the surface of nanosheets in HCPS-10-400 becomes rough and re-stacking (Figure S3c and S3d).

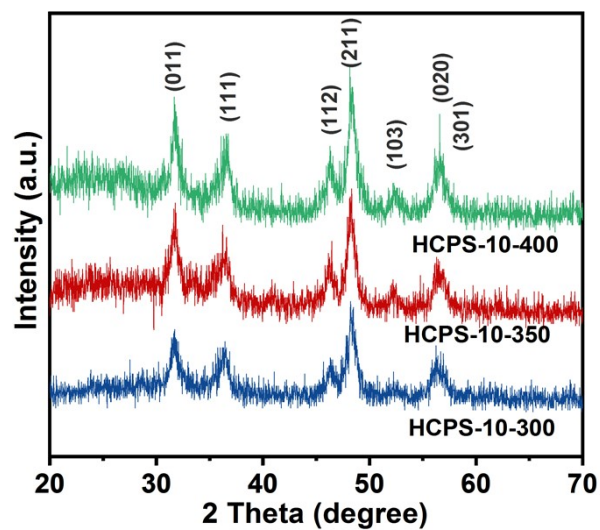


Figure S4. XRD patterns of HCPS-10-300, HCPS-10-350 and HCPS-10-400.

Figure S4 exhibits the XRD patterns of the CoP-based samples obtained at different phosphorization temperatures. In Figure S4, the intensity of peaks become stronger in the order of HCPS-10-300, HCPS-10-350 and HCPS-10-400, suggesting that the crystallinity elevates with the increase of phosphating temperature.

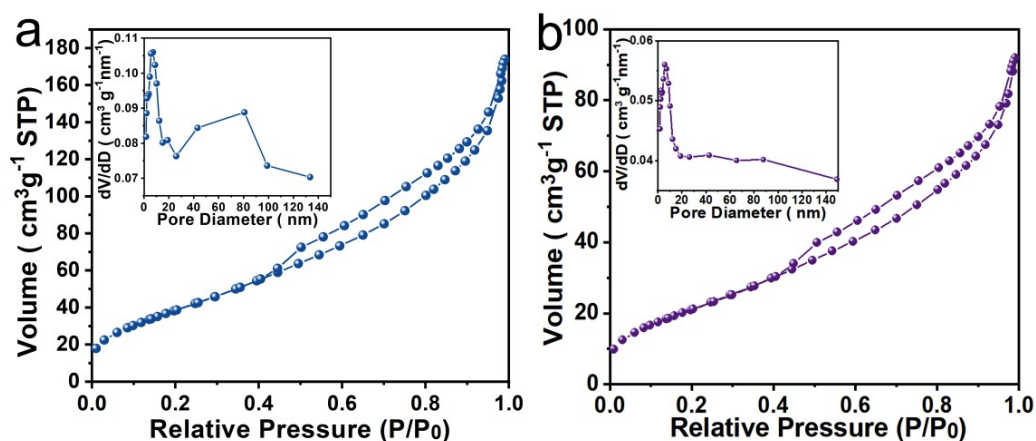


Figure S5. N₂ adsorption/desorption isotherms and pore size distribution (inset) of (a) HCPS-10-300 and (b) HCPS-10-400.

The N₂ adsorption/desorption isotherm and pore-size-distribution (PSD) curves of as-fabricated samples are depicted in Figure S5. The BET surface areas of HCPS samples increase from 142.5 m² g⁻¹ to 160.2 m² g⁻¹ with an increase of temperature from 300 to 350 °C, ascribing to the formation of pores by the release of H₂O from Co-EG precursor at elevated temperature. And then drops to 78.3 m² g⁻¹ as the temperature up to 400 °C, indicating the degradation of the structure. Therefore, the BET results indicate that the active areas of HCPS materials can be adjusted by turning the phosphating temperature.

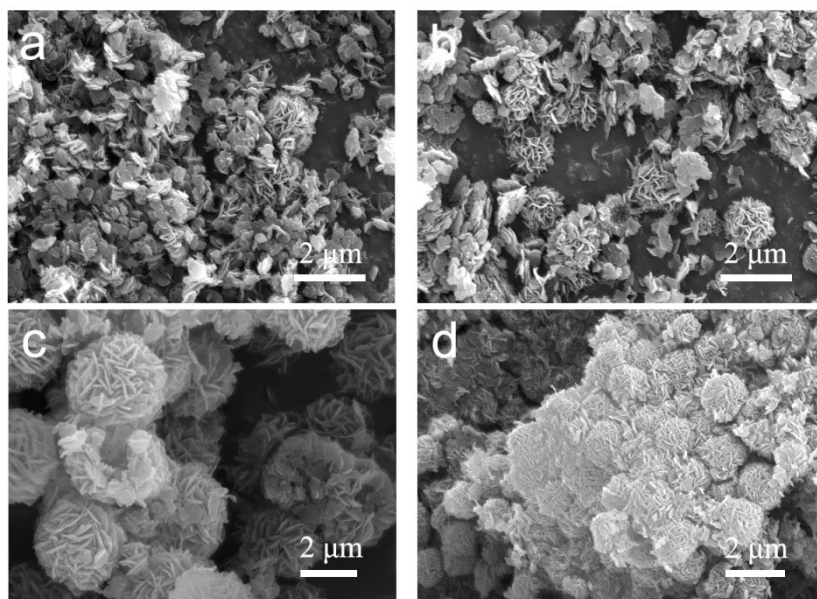


Figure S6. SEM images of (a) Co-EG-4, (b) Co-EG-6, (c) Co-EG-8 and (d) Co-EG-12.

To study the formation process of the precursor and finally adjust the structure of the phosphides, we have tuned the parameters during the synthesis of the precursor. A range of samples were achieved with different solvothermal times for 4h, 6h, 8h, 10h and 12h, respectively. SEM analyses verified the evolutionary process of the hierarchical hollow structure. The small nanosheets can be appeared during the first 4 hours (Figure S6a). With solvothermal time up to 6 hours, the partial nanosheets can tend to assemble into hollow microspheres, for which both nanosheets and hollow microspheres can be seen (Figure S6b). When the solvothermal time is extended to 8 hours, the SEM image (Figure S6c) shows the majority of hollow spheres. Further increasing the time to 10h, only presents well-dispersed 3D hollow spheres composed with 2D nano-sheet units (Figure 2b). As the time is elevated to 12h, the hollow spheres were partly collapse (Figure S6d). The above analyses indicate the important effect of solvothermal time on the formation of the precursor, which can in turn regulate the morphology of final phosphides and their capacitive property.

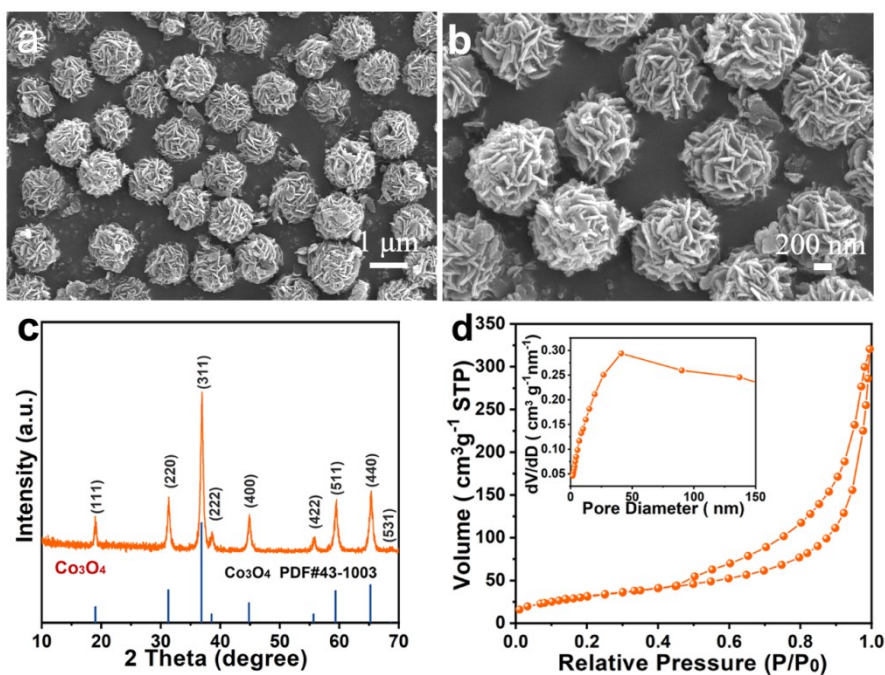


Figure S7. (a, b) SEM images, (c) XRD pattern and (d) N₂ adsorption/desorption isotherm and pore size distribution (inset) of the Co₃O₄.

In order to better study the merits of HCPS materials as an electrode for the supercapacitors, Co₃O₄ was prepared in the absence of P source (NaH₂PO₂) by heating Co-EG-10 precursor at 350 °C in air atmosphere. The structural feature of Co₃O₄ is described as follows. The morphology of Co₃O₄ was first investigated by SEM. As observed in Figure S7a and S7b, Co₃O₄ presents hollow spheres consisting of many nanosheet arrays with an average diameter of about 1 μm. Moreover, the XRD pattern (Figure S7c) shows the crystalline characteristics of Co₃O₄. The diffraction peaks were indexed to phases of Co₃O₄ (PDF#43-1003). In addition, the Co₃O₄ displays the Brunauer-Emmett-Teller surface area of 154.2 m² g⁻¹ (Figure S7d). SEM analyses and N₂ adsorption/desorption isotherm tests illustrated that the microstructure and BET surface area of Co₃O₄ are similar to those of HCPS-10-350.

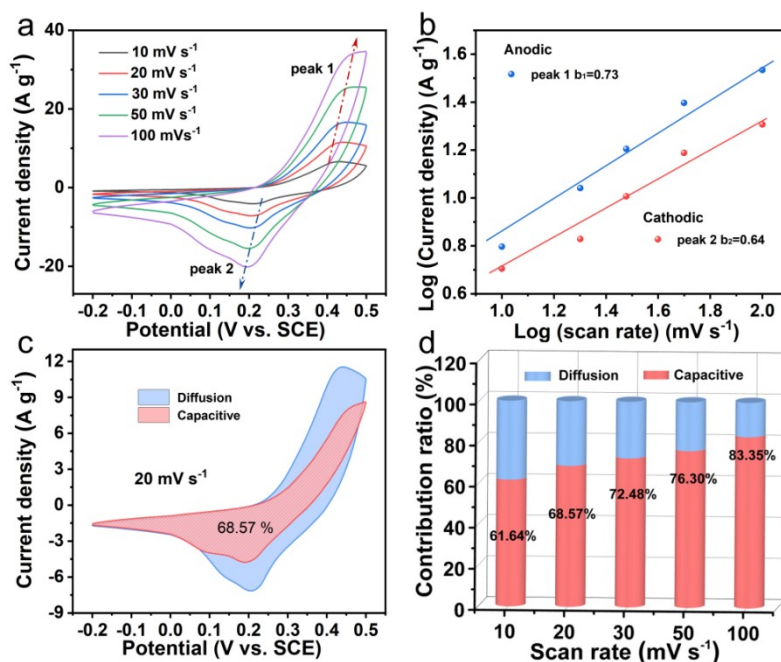


Figure S8. Electrochemical performance of the Co_3O_4 using a three-electrode system in 2 M KOH electrolyte: (a) CV curves of Co_3O_4 electrode at various scan rate from 10 mV s^{-1} to 100 mV s^{-1} ; (b) The plot of $\log i$ vs $\log v$ of Co_3O_4 electrode at different redox states; (c) Capacitive and diffusion-controlled charge storage contribution of Co_3O_4 electrode at 20 mV s^{-1} ; (d) Charge storage contribution ratio of at different scan rates for Co_3O_4 electrode.

The CV curves of Co_3O_4 electrode at different scan rates of $10\text{-}100 \text{ mV s}^{-1}$ were performed to assess capacitive behavior of Co_3O_4 electrode. In Figure S8a, the obvious redox peaks at around $0.41/0.20 \text{ V}$ can be observed, resulted from the redox reaction of $\text{Co}^{2+}/\text{Co}^{3+}$. Importantly, the shape of the CV curve undergoes slight distorted at a scan rate as high as 100 mV s^{-1} . Besides, the kinetic behavior of Co_3O_4 electrode is evaluate by fitting the CV curves under various scan rate according power-law equation. As demonstrated in Figure S8b, the b values of Co_3O_4 electrode are 0.73 and 0.64 , which shows that the capacitance is more derived from the capacitive-controlled behavior. Moreover, the capacitive contribution of Co_3O_4 electrode increases from 61.64% to 83.35% as the scan rate from 10 mV s^{-1} to 100 mV s^{-1} (Figure S8c and S8d), further indicating that the charge storage mechanism of Co_3O_4 electrode is mainly dominated by a capacitive-controlled process.

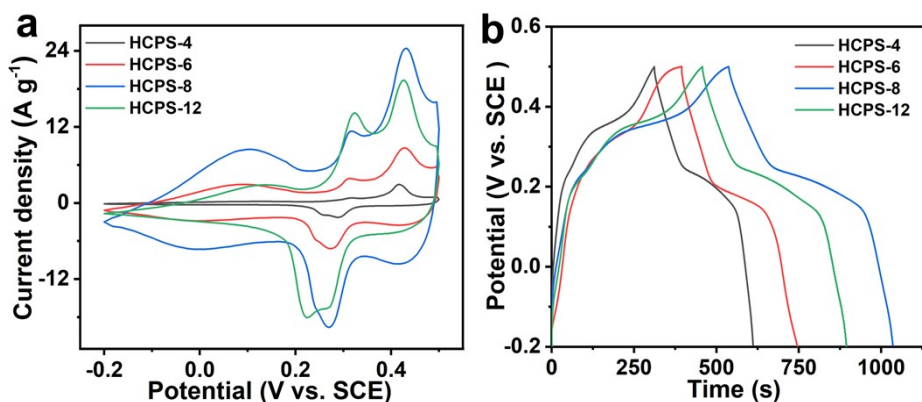


Figure S9. (a) CV curves of HCPS-4, HCPS-6, HCPS-8 and HCPS-12 at 20 mV s^{-1} in the voltage range of $-0.2\sim 0.5 \text{ V}$; (b) GCD curves of HCPS-4, HCPS-6, HCPS-8 and HCPS-12 at 1 A g^{-1} in the voltage range of $-0.2\sim 0.5 \text{ V}$.

To gain insight into the structure-performance relationships, the capacitive behavior of the precursors from different solvothermal time after phosphoring is also studied. The CV curves of HCPS-4, HCPS-6, HCPS-8 and HCPS-12 at 20 mV s^{-1} as shown in Figure S9a. All of as-made electrodes present observed obvious faradaic redox peaks, indicating a faradaic behavior. Moreover, the products with different solvothermal time after phosphoring display different capacitive properties. The specific capacitance of as-prepared products was calculated from GCD curves (Figure S9b). With increasing solvothermal time, the capacitances firstly increase from HCPS-4 (428 F g^{-1}) to HCPS-10-350 (723 F g^{-1}), then decrease to HCPS-12 (625 F g^{-1}). The results demonstrated that the capacitive behavior of the electrode materials can be tuned by adjusting the micro-structure of the phosphides.

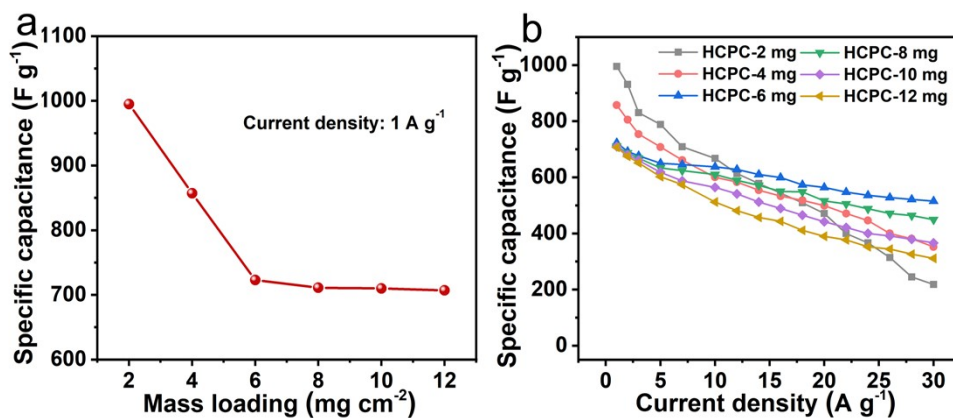


Figure S10. (a) Specific capacitance of the HCPS-10-350 coated Ni foam electrodes as a function of the mass loading of HCPS-10-350 sample; (b) Specific capacitance as a function of current density ranging from 1 to 30 A g⁻¹.

The active electrode with a high loading is an important factor in the practical application. Generally, the capacitance and rate capability can be decreased with an increase in mass loading of active materials, which has prevented its wide applications. material, To maximize the capacity at high mass loading, the HCPS-10-350 electrodes with different loading amount from 2 mg cm⁻² to 12 mg cm⁻² were also prepared to study relationship between mass loading and rate behaviors (Figure S10a). it can be shown that the specific capacitance gradually decreased from 995 F g⁻¹ (HCPS-2mg) to 723 F g⁻¹ (HCPS-6mg) with increasing the mass loading of active material until the mass achieved to 6 mg cm⁻². With the further increase of loading, the specific capacitance have no obvious change. The capacitance plot of these electrodes at different current density were also performed to investigate the rate behaviors (Figure S9b). The HCPS-6mg exhibits the highest capacitance retention of 71.21 % superior to other as-made samples. The above results indicated that the ideal mass loading in this work reach up to 6 mg due to its both high rate capability and suitable high capacitance. The excellent capacitance behavior at large mass loading is depended by the high conductivity of the CoP and hollow architecture assembled by porous nanosheets.

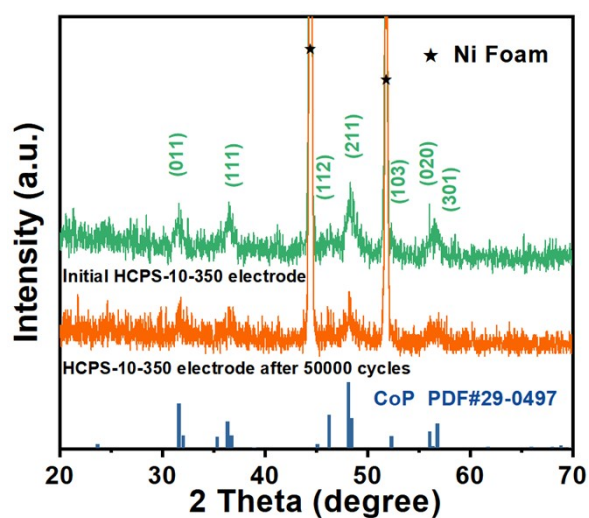


Figure S11. XRD patterns of the HCPS-10-350 coated on Ni foam before and after 50,000 GCD cycles.

The crystal phase of HCPS-10-350 electrode before and after 50,000 GCD cycles was examined by XRD. As observed in Figure S11, the crystal structure of the HCPS-10-350 electrode after 50,000 cycles is similar to that of the original HCPS-10-350. However, the intensities of diffraction peaks indexed to CoP is decreased due to the formation of an oxy-hydroxide phase on the surface of the CoP, which leads to the generation for a new active phase of the CoOOH.

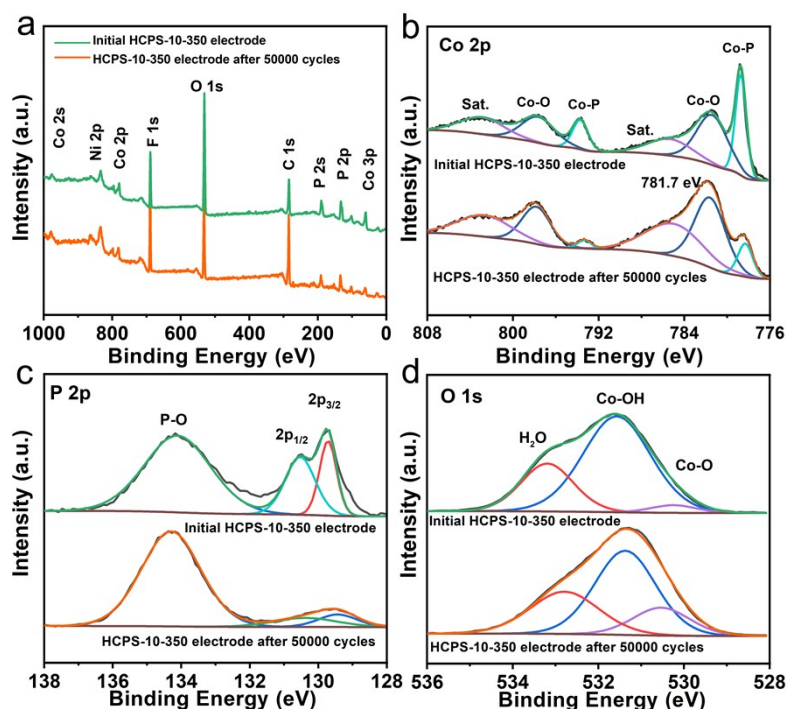


Figure S12. (a) Survey XPS spectra of the HCPS-10-350 coated on Ni foam before and after 50,000 GCD cycles, the high-resolution XPS spectra of (b) Co 2p, (c) P 2p and (d) O 1s of the HCPS-10-350 coated on Ni foam before and after cycling.

The chemical state changes of HCPS-10-350 after cycling were investigated by the X-ray photoelectron spectroscopy (XPS). The survey XPS spectra (Figure S12a) clearly indicate the presence of Co, Ni, P, O, F and C elements in both HCPS-10-350 before and after cycles, in which the examined Ni, F and C elements should be mainly derived from Ni foam and binder (polytetrafluoroethylene, PTFE). Figure S12b has displayed the Co 2p spectra of HCPS-10-350 before and after 50,000 GCD cycles. Compared with initial HCPS-10-350, the peaks correspond to the Co-P bonds decline and have a little shift to higher binding energy, which further indicate that CoP is partly converted to amorphous CoOOH, whereas the certain CoP phase is preserved after 50,000 cycles. Moreover, the P 2p spectra of HCPS-10-350 before and after the stability test shown in Figure S12c, the peak located at 129.4 and 130.2 eV can be decreased after cycling, indicating the transform from CoP to CoOOH. Thus, the capacitance retention firstly increases owing to the

generation of new active phase of the CoOOH on the surface of the CoP during the initial cycles. The above results have shown that the major contribution to the high long-term cycling stability can be mainly ascribed to oxyhydroxide phase generated on the surfaces and better electronic conductivity of the CoP.

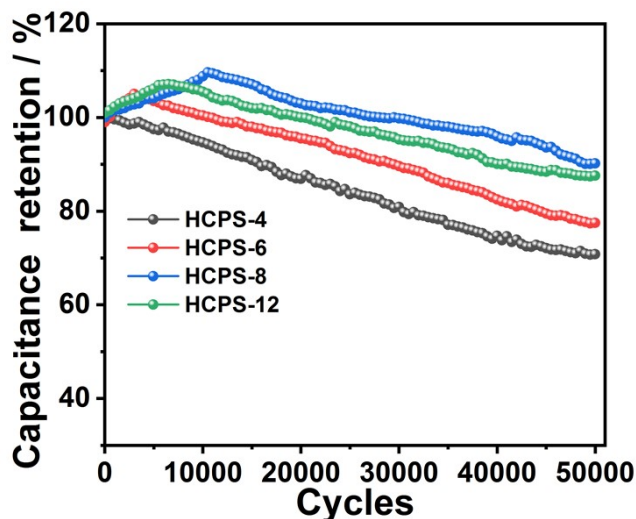


Figure S13. The cycle stability of the HCPS-4, HCPS-6, HCPS-8 and HCPS-12 electrode measured at a current density of 10 A g^{-1} for 50000 cycles.

The high cycling performance was closely related to the structure of the HCPS-based electrode materials. Thus, the cycling performance of precursors made using different hydrothermal times after phosphatization as the compared samples were constructed under the same conditions. As shown in Figure S13, the capacitance retention of HCPS-4, HCPS-6, HCPS-8 and HCPS-12 are 70.8 %, 77.5 %, 90.2 % and 87.9 %, respectively, which are lower than that of HCPS-10-350 electrode (94.3 %). The results indicated that HCPS-10-350 has the highest stability, suggesting the benefit of its hollow structure assembled by porous nanosheets for promoting electrochemical stability.

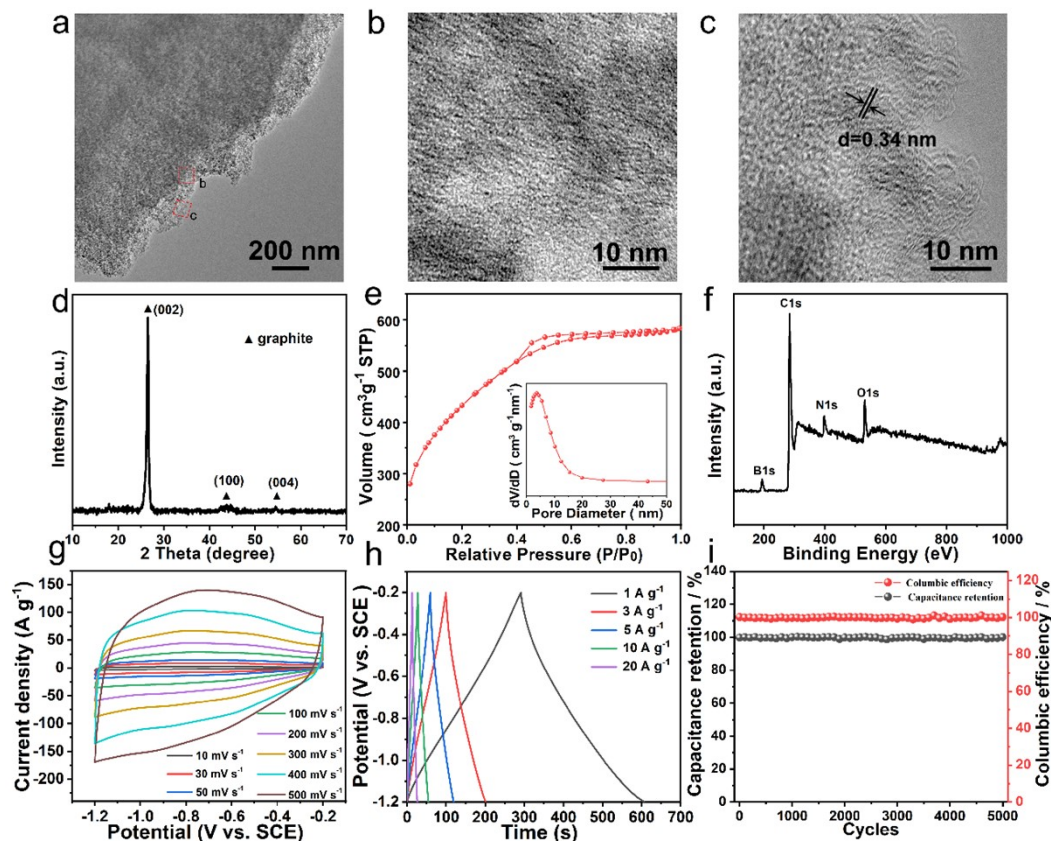


Figure S14. The structural and capacitive analyses for BNGC electrode material: (a) TEM image of BNGC; (b,c) HRTEM images of selected areas of (a); (d) XRD patterns of BNGC; (e) N₂ adsorption/desorption isotherm and pore size distribution (inset) of BNGC; (f) Survey XPS spectrum of BNGC; (g) CV curves of BNGC at various scan rate from 10 mV s⁻¹ to 500 mV s⁻¹; (h) GCD curves of BNGC at different current densities from 1 A g⁻¹ to 20 A g⁻¹; (i) Cycle stability and Coulombic efficiency of the CoP-10-350 electrode for 5000 cycles measured at 10 A g⁻¹.

Here, we used B, N-doped graphitic carbon (BNGC) as negative electrode for ASC device. In detail, the nanostructure of BNGC was studied by TEM, XRD, XPS and N₂ adsorption/desorption tests. Figure S14a displays TEM image of BNGC. As shown in Figure S14a, BNGC presents a sheets-like structure with continuous nanopores. Figure S14b and S14c show HRTEM images of the selected regions in Figure S14a. Figure S14b indicated that BNGC has vast interconnected micropores. From Figure S14c, it can be found that the lattice fringe spacing is about 0.34 nm, which corresponds to the graphite (002) plane, implying a graphitic structure of BNGC. The crystal structure of the BNGC was identified via powder XRD analysis. the

diffraction peak (Figure S14d) at 26.5° can be assigned as the (002) plane of graphite, further revealing the high crystallinity of BNGC. N_2 adsorption/desorption isotherm was also conducted to survey the specific surface area and pore structures of BNGC. As shown in Figure S14e, the BET surface area for BNGC was calculated to be $1567 \text{ m}^2 \text{ g}^{-1}$. Moreover, the XPS survey spectrum of BNGC indicated the presence of carbon, nitrogen, boron, and oxygen atoms without evidence of impurities. Based on the above experimental analyses, BNGC have good conductivity, a large surface area and isolated boron and nitrogen centers after co-doping. The unique structure make BNGC displays high capacitance of 313 A g^{-1} at 1 A g^{-1} , high rate property (83.1 % at 20 A g^{-1}) and also long-term durability and Coulombic efficiency of $>99.5\%$ (Figure S14g, S14h and S14i).

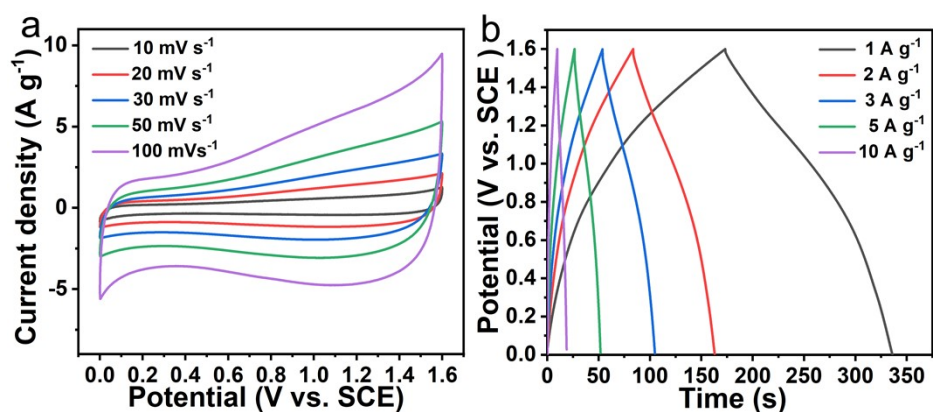


Figure S15. (a) CV curves of Co₃O₄//BNGC ASC device at scan rate from 10 mV s⁻¹ to 100 mV s⁻¹. (b) GCD curves of Co₃O₄//BNGC ASC device at current densities from 1 A g⁻¹ to 10 A g⁻¹.

Figure S15a exhibits the CV curves of the Co₃O₄//BNGC ASC device at different scan rates from 10 to 100 mV s⁻¹. The shape of CV curves does not change obviously with the increase of scan rate, indicating that the assembled ASC has good reversibility during the charge-discharge process. The specific capacitance at 1, 2, 3, 5 and 10 A g⁻¹ calculated from Figure. 15b are 101.7, 99.5, 96.4, 79 and 56.7 F g⁻¹ respectively. 55.75% capacitance is retained as the current density increases from 1 to 10 A g⁻¹, which is lower than that of HCPS-10-350//BNGC ASC device (76.46 %). Therefore, although the Co₃O₄//BNGC ASC device have excellent reversibility, the rate capability still hinder its large-scale commercial application.

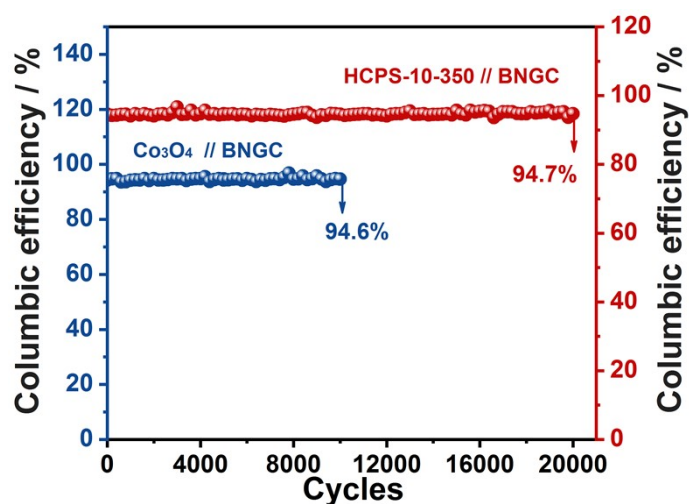


Figure S16. Coulombic efficiency of the HCPS-10-350//BNGC and Co₃O₄//BNGC ASC device at 10 A g⁻¹ after 20000 and 10000 cycles, respectively.

The coulombic efficiency of the ASC device were calculated based on GCD curves (Figure S16). The coulombic efficiency of HCPS-10-350//BNGC ASC device still maintains as high as 94.7 % at 10 A g⁻¹ after 20000 cycles, while the coulombic efficiency for Co₃O₄//BNGC ASC device achieves 94.6 % at 10 A g⁻¹ after 10000 cycles. The analysis demonstrated good reversibility of HCPS-10-350//BNGC ASC device.

Table S1. The as-prepared samples and their corresponding synthesis parameters.

| Entry | Starting materials | Cobalt acetate (mmol) | solvothermal Temperature (°C) | Solvothermal Time (h) | Phosphorization Temperature (°C) | Final samples |
|-------|--------------------|-----------------------|-------------------------------|-----------------------|----------------------------------|---------------|
| 1 | Co-EG-4 | 2 | 180 | 4 | 350 | HCPS-4 |
| 2 | Co-EG-6 | 2 | 180 | 6 | 350 | HCPS-6 |
| 3 | Co-EG-8 | 2 | 180 | 8 | 350 | HCPS-8 |
| 4 | Co-EG-10 | 2 | 180 | 10 | 350 | HCPS-10-350 |
| 5 | Co-EG-12 | 2 | 180 | 12 | 350 | HCPS-12 |
| 8 | Co-EG-10-300 | 2 | 180 | 10 | 300 | HCPS-10-300 |
| 9 | Co-EG-10-400 | 2 | 180 | 10 | 400 | HCPS-10-400 |

Table S2. Textual parameters of the as-fabricated Co-based samples.

| Sample | S_{BET} (m^2g^{-1}) | Pore volume (cm^3g^{-1}) | Pore size (nm) |
|-------------------------|--|--|----------------|
| Co-EG-10 | 86.2695 | 0.17436 | 7.3594 |
| HCPS-4 | 44.2687 | 0.15488 | 12.0255 |
| HCPS-6 | 72.4262 | 0.270162 | 14.7053 |
| HCPS-8 | 90.8701 | 0.259349 | 15.3774 |
| HCPS-10-350 | 160.2167 | 0.265230 | 16.4102 |
| HCPS-12 | 135.2898 | 0.279993 | 10.3884 |
| HCPS-10-300 | 142.5273 | 0.181186 | 7.1880 |
| HCPS-10-400 | 78.2667 | 0.0941 | 6.9271 |
| Co_3O_4 | 154.2368 | 0.2925 | 14.3578 |

Table S3. Specific capacitances of the studied samples calculated from discharge curves measured at different current densities.

| Sample | C (F g ⁻¹) | | | | | | |
|--------------------------------|------------------------|------------------------|------------------------|------------------------|------------------------|------------------------|------------------------|
| | 1 (A g ⁻¹) | 2 (A g ⁻¹) | 3 (A g ⁻¹) | 5 (A g ⁻¹) | 10(A g ⁻¹) | 20(A g ⁻¹) | 30(A g ⁻¹) |
| Co-EG-10 | 355 | 337 | 312 | 297 | 259 | 124 | 72 |
| HCPS-4 | 428 | 374 | 347 | 322 | 296 | 257 | 216 |
| HCPS-6 | 505 | 489 | 443 | 385 | 322 | 291 | 271 |
| HCPS-8 | 712 | 672 | 635 | 586 | 521 | 483 | 467 |
| HCPS-10-350 | 723 | 692 | 677 | 650 | 637 | 564 | 515 |
| HCPS-12 | 625 | 590 | 561 | 526 | 480 | 435 | 384 |
| HCPS-10-300 | 685 | 664 | 646 | 633 | 597 | 488 | 395 |
| HCPS-10-400 | 672 | 653 | 638 | 616 | 584 | 517 | 432 |
| Co ₃ O ₄ | 561 | 543 | 530 | 496 | 453 | 368 | 227 |

Table S4. Comparison of supercapacitive performance of HCPS-10-350 with other previously reported CoP-based electrodes using a three-electrode system.

| Electrode materials | capacitance | voltage | Capacity retention | Cycling stability | Ref |
|---|---|----------------|---|---|---|
| HCPS-10-350 | 723 F g ⁻¹ at 1 A g ⁻¹ | -0.2~ 0.5V | 88.1% from 1 to 10 A g ⁻¹ and 71.21% from 1 to 30 A g ⁻¹ | 112.7% after 10k cycles at 10 A g ⁻¹ and 94.3% after 50k cycles at 10 A g ⁻¹ | This work |
| Co(P, S)/CC | 610 F g ⁻¹ at 1 A g ⁻¹ | -0.2~ 0.45V | 56% from 1 to 10 A g ⁻¹ | 99% after 10k cycles at 10 A g ⁻¹ | Nano Energy, 2017 , 39, 162 |
| CoP-NPC/GS | 166 F g ⁻¹ at 3 A g ⁻¹ | -0.1~ 0.4V | 83% from 3 to 15 A g ⁻¹ | 88% after 10k cycles at 7 A g ⁻¹ | J. Colloid Interf. Sci., 2021 , 582,1136 |
| CoP nanowires /CC | 674 F g ⁻¹ at 5 mV s ⁻¹ | 0~0.6V | 31.7% from 5 to 200 mV s ⁻¹ | 86 % after 3k cycles at 10 mA cm ⁻¹ | Sci China Mater, 2017 ,60,1179 |
| CoP microcubes | 560 F g ⁻¹ at 1 A g ⁻¹ | 0~0.6V | 69% from 0.5 to 8 A g ⁻¹ | 91.2% after 10k cycles at 5 A g ⁻¹ | Inorg. Chem., 2018 , 57, 10287 |
| CoP-Ni ₂ P/NF | 1.43 C cm ⁻² at 1 mA cm ⁻¹ | 0~0.4V | 60.84% from 1 to 10 mA cm ⁻¹ | 43.7 % after 5k cycles at 10 mA cm ⁻¹ | Nanoscale, 2020 ,12, 20710 |
| CoP nanowires | 558 F g ⁻¹ at 1 A g ⁻¹ | 0~0.6V | 73% from 1 to 20 A g ⁻¹ | 98% after 5k cycles at 2 A g ⁻¹ | Colloid Surf. A, 2018 , 553, 58 |
| Co ₂ P nanoshuttle | 246 F g ⁻¹ at 1 A g ⁻¹ | -0.2~ 0.3V | 72% from 1 to 20 A g ⁻¹ | 72% after 1k cycles at 2 A g ⁻¹ | CrystEngComm, 2018 , 20, 2413. |
| Ni-CoP@C@CNT | 708.1F g ⁻¹ at 1 A g ⁻¹ | 0~0.6V | 62.7% from 1 to 20 A g ⁻¹ | 76.1% after 3k cycles at 5 A g ⁻¹ | Chem. Eng. J. 2020 , 385, 123454 |
| Hollow Co ₂ P nanoflowers | 412.7 F g ⁻¹ at 1 A g ⁻¹ | -0.2~ 0.6V | 64.6% from 1 to 20 A g ⁻¹ | 124.7 % after 10k cycles at 5 A g ⁻¹ | Nanoscale, 2017 , 9, 14162 |
| CoP nanoparticle | 447.5 F g ⁻¹ at 1 A g ⁻¹ | -0.2~ 0.6V | 70.3% from 1 to 10 A g ⁻¹ | 84.3% after 5k cycles at 2 A g ⁻¹ | J. Energy Chem., 2017 , 26, 49 |

Table S5. Comparison of vital capacitive parameters indexes of HCPS-10-350// BNGC ACS device with other previously reported Co-based ACS device.

| ASC device | Energy density | Power density | Capacity retention | Cycling stability | Ref |
|--|--|--|--|--|--|
| HCPS-10-350 //BNGC | 50.67 Wh kg ⁻¹ 38.72 Wh kg ⁻¹ | 800 W kg ⁻¹ 8000 W kg ⁻¹ | 76.5% from 1 to 10 A g ⁻¹ 54.9% from 1 to 30 A g ⁻¹ | 99.8% after 10k cycles at 10 A g ⁻¹ 96.2% after 20k cycles at 10 A g ⁻¹ | This work |
| CoP//FeP ₄ | 46.38 Wh kg ⁻¹ 34.22 Wh kg ⁻¹ | 695 W kg ⁻¹ 7001 W kg ⁻¹ | 73.3% from 1 to 10 A g ⁻¹ | 89% after 10k cycles at 10 A g ⁻¹ | Small, 2021 ,17, 2007062 |
| pompon-like CoP//AC | 22.2 Wh kg ⁻¹ 13 Wh kg ⁻¹ | 374.9 Wh kg ⁻¹ 6000 W kg ⁻¹ | 58.5% from 0.5 to 8 A g ⁻¹ | 80.9% after 3k cycles at 2 A g ⁻¹ | Electrochim. Acta, 2019 , 299, 62 |
| CoP arrays // CMK-3 | 19 Wh kg ⁻¹ | 1333 W kg ⁻¹ | 53% from 0.3 to 3 A g ⁻¹ | 93% after 5k cycles at 10 A g ⁻¹ | Appl. Surf. Sci.57 2020 , 527, 146682 |
| CoP/NiCoP //AC | 31.1 Wh kg ⁻¹ | 8000 W kg ⁻¹ | 60.3% from 1 to 10 A g ⁻¹ | 95% after 3.2k cycles at 10 A g ⁻¹ | Adv. Energy Mater. 2019 , 9, 1901213 |
| NiCoP@CoS //AC | 28.5 Wh kg ⁻¹ | 7489.1 W kg ⁻¹ | 79.5% from 1 to 10 A g ⁻¹ | 86.1% after 10k cycles at 10 A g ⁻¹ | Chem. Eng. J. 2021 ,2021, 421 , 127871 |
| Ni-Co-P/PO _x //RGO | 19.87 Wh kg ⁻¹ | 5670 W kg ⁻¹ | 69.2% from 0.3 to 3 A g ⁻¹ | 86% after 7k cycles at 3 A g ⁻¹ | J. Mater. Chem. A, 2019 ,7,6241 |
| CeO ₂ @CoP //AC | 34.9 Wh kg ⁻¹ | 4800 W kg ⁻¹ | 63% from 1.2 to 6 A g ⁻¹ | 89% after 5k cycles at 5 mA cm ⁻² | Electrochim. Acta, 2020 , 337, 135817 |
| CoP@NiCoP //Fe ₂ O ₃ | 37.16 Wh kg ⁻¹ | 875 W kg ⁻¹ | 50.23% from 1 to 5 A g ⁻¹ | 50% after 1k cycles at 10 A g ⁻¹ | Appl. Surf. Sci. 2020 , 532, 147437 |
| Mn-doped Co ₃ O ₄ //AC | 20.6 Wh kg ⁻¹ | 16000 W kg ⁻¹ | 42.7% from 0.5 to 10 A g ⁻¹ | 86% after 2k cycles at 3 A g ⁻¹ | Chem. Eng. J. 2021 ,421,129767 |
| P-Ni(OH) ₂ @ Co(OH) ₂ /NF //Fe ₂ O ₃ /CC | 0.11mWh cm ⁻² | 16 mW cm ⁻² | 50.5% from 1 to 10 mA cm ⁻² | 81% after 5k cycles at 20 mA cm ⁻² | Small, 2020 ,16, 2001974 |
| NiCoMn-S //RGO | 42.1 Wh kg ⁻¹ | 750W kg ⁻¹ | 31.6% from 1 to 30 A g ⁻¹ | 88.7% after 10k cycles at 7 A g ⁻¹ | Chem. Eng. J. 2021 ,405,126928 |